Environmental Science Advances

ROYAL SOCIETY OF CHEMISTRY

PAPER

View Article Online
View Journal | View Issue

Cite this: *Environ. Sci.: Adv.*, 2026, **5**, 485

Multifunctional lignin biocomposite for broad-spectrum water purification

Sritama Mukherjee, *[a] Salvatore Lombardo [b] and Ulrica Edlund *[a]

Received 21st August 2025
Accepted 6th December 2025

DOI: 10.1039/d5va00282f

rsc.li/esadvances

Removal of heavy metal ions, PFAS, and synthetic dyes from anthropogenic wastewater using versatile sustainable materials is of prime importance for a clean environment and human health. This study presents a sustainably engineered lignin-based biocomposite reinforced with chitosan, designed for multifunctionality, enhanced material performance, and produced *via* a 'green' and simple one-pot synthesis in aqueous medium. The synthesized granular material, *i.e.* a zwitterionic lignin-chitosan composite (ZLC), was used for the removal of a wide range of chemically diverse contaminants. ZLC showed 80–90% removal of heavy metals such as Cr(VI), Cu(II), and four different cationic and anionic dyes. It was also tested against an array of five PFAS molecules, such as perfluorinated sulfonic and carboxylic acids, showing up to 86% removal for perfluorooctane sulfonic acid (PFOS). All adsorption processes followed the pseudo-second order and Langmuir models. The material also showed antifouling behavior, demonstrating robustness for real-time application. Lastly, ZLC was tested against effluent water matrices, *i.e.*, wastewater streams from mining areas located in Sweden. The multifunctional adsorption performance of the environment-friendly material, coupled with its ease of production, cost effectiveness, and reusability, indicates that ZLC has a high potential that can garner industrial interest for simplifying multi-step filtration processes.

Environmental significance

The release of persistent organic pollutants such as PFAS, synthetic dyes, and toxic metals into aquatic systems presents an escalating environmental concern. Addressing the dominating flow of miscellaneous pollutants into the environment requires a sustainable and multifunctional technology. We report a bio-derived adsorbent – functionalized lignin-chitosan composite (ZLC), that achieved 80–90% removal of diverse pollutants, with performance maintained through multiple regeneration cycles and antifouling properties. Leveraging the natural abundance and functionality of lignin and chitosan, ZLC represents a promising platform for scalable, recyclable, and environmentally benign water purification, contributing to the development of sustainable contaminant remediation strategies.

1 Introduction

With the ever-growing water consumption in agriculture, industry, energy, and municipal areas, along with a limited supply of natural freshwater, it is necessary to shift towards using nontraditional water sources such as wastewater, seawater, and brackish water. Safe use of these sources requires water treatment systems that can remove nearly all dissolved constituents from contaminated water. Untreated wastewater from anthropogenic sources such as waste streams from mining areas and various industries, when released into surface water and groundwater, poses risks to drinking water safety for millions of people.[1] The presence of various toxic contaminants like organic micropollutants, heavy metal ions, forever chemicals such as per- and polyfluorinated substances (PFAS), *etc.*, even at low concentrations, can be a major contributor to water-related diseases.[2] PFAS has caught attention due to its thousands of variations that are difficult to break down naturally and have widespread industrial applications, thus leading to its rampant mobilization to water, soil, and wildlife.[3] Primary examples of this category include perfluorinated alkyl carboxylic and sulfonic acids, notably perfluorooctanoic acid (PFOA) and perfluorooctane sulfonic acid (PFOS), whose production and utilization are now globally prohibited, leading to the emergence of alternative per- and polyfluoroalkyl substances with analogous characteristics.[4,5] The remarkable stability of the C–F bond precludes both biological and abiotic degradation, resulting in persistent perfluorinated residues despite the transformation of certain non-fluorinated precursors, which compels the regulatory bodies to set stricter levels. These scenarios underscore the urgency for the development of

[a]*Department of Fiber and Polymer Technology, School of Chemistry, Biotechnology and Health, KTH Royal Institute of Technology, Stockholm 10044, Sweden. E-mail: sritama@kth.se; edlund@kth.se*

[b]*Department of Materials and Environmental Chemistry, Stockholm University, Stockholm 10691, Sweden*

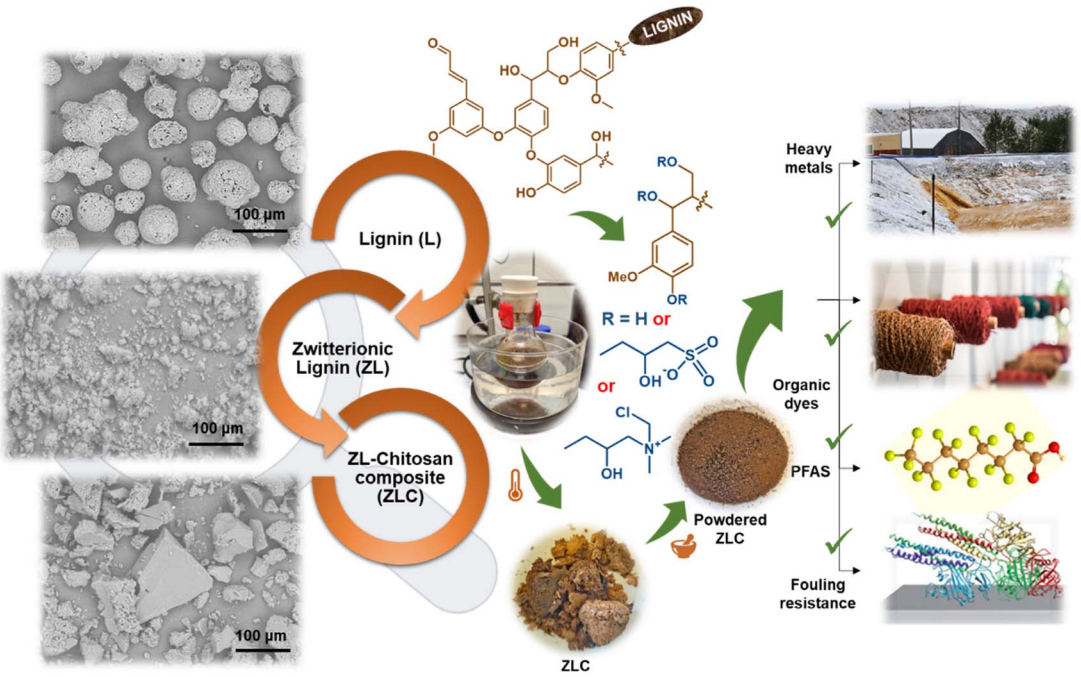

Fig. 1 A schematic illustration of the process of functionalization of lignin and its composite formation with chitosan, along with the corresponding SEM images of the lignin precursor, ZL and ZLC granules, followed by their application for treating chemically diverse water contaminants such as heavy metals, organic dyes, PFAS molecules, and biofouling.

'smart' materials, leading to technological advancements that can facilitate access to clean water from alternative sources.[6]

The conventional methods for water and wastewater treatment are often characterized by high levels of chemical, energy, and operational requirements, focusing on large-scale systems.[7] Adsorptive materials see a wide-scale usage as they exhibit improved performance in numerous separations when compared with conventional technologies, in terms of capacity, selectivity, regenerability, and affordability.[8] Polymer-derived materials, particularly biopolymers, can largely improve advanced adsorption processes from technical, socioeconomic, and environmental perspectives.

Lignin is a major structural component of lignocellulosic biomass and playing a vital role in the composition of terrestrial plant biomass.[9] The lignin polymer is largely composed of three phenylpropanoid subunits: *p*-hydroxyphenyl (H), guaiacyl (G), and syringyl (S), and the total carbon content accounts for *ca.* 60% of its structure.[10] Lignin is rich in hydroxyl groups, which significantly influence its chemical and physical characteristics, including reactivity, hydrophilicity, and functionality. Chitosan is another bio-derived polymer having an amino polysaccharide structure and is well known for its versatile applicability. Both lignin and chitosan allow a wide array of chemical modifications, facilitated by their solubility in various solvents, enabling the introduction of various functional groups onto their aromatic rings and hydroxyl groups.[11] Lignin and chitosan are, therefore, both from an environmental and a chemical perspective, interesting candidates for water purification materials.

Designing a multifunctional material with high adsorption capacity for a broad range of contaminants presents a significant scientific challenge due to several factors stemming from the complexity and diversity of common pollutants. Contaminants can be polar, non-polar, or amphiphilic, and they have various functional groups that interact differently with adsorbent materials. They also vary significantly in size, from small ions to large organic molecules or even nanoparticles, requiring adsorbent materials with pore sizes that can accommodate this wide range. Furthermore, achieving efficient adsorption for diverse contaminants is challenging because enhancing selectivity for one type of contaminant may reduce efficiency for others. Multifunctional materials can simplify multi-step filtration processes in water treatment industries. An ideal versatile adsorbent material must have sites that can attract and hold anionic, cationic, and neutral species effectively across a range of pH levels and offer a pore structure that can accommodate different contaminant sizes. From this perspective, zwitterionic moieties immobilized within a porous matrix stand out as an interesting approach for an adsorbent with the capacity to exert electrostatic interaction with anionic as well as cationic entities simultaneously. Zwitterionic membranes have been shown to effectively suppress bacterial and protein fouling and attract heavy metal ions.[12–14] A soluble fraction of kraft lignin functionalized with zwitterionic groups showed excellent protein repellent properties.[15] Few preliminary studies reported the making of chitosan-lignin composites, but with limited applicability for selective metal or dye removal.[16,17] Materials offering effective broad-spectrum treatment are rare.

Keeping it as motivation, we present a proof-of-concept study where alkali lignin is functionalized to have zwitterionic groups and is subsequently reinforced with chitosan to produce

a biocomposite using a simple and green one-pot synthetic process. While the functionalized lignin provides active sites for adsorbing and holding anionic, cationic, and neutral chemically diverse species effectively, chitosan reinforcement renders mechanical strength and stability across a range of pH levels and diverse environmental conditions, alongside avoiding biofouling synergistically, thereby making it robust for real-world applications. We developed the zwitterionic lignin biocomposite (ZLC), a versatile antifouling material for capturing a wide range of contaminants such as heavy metal ions, cationic and anionic dyes, and PFAS molecules. The processing and application of zwitterion-type lignin (ZL) and ZLC are schematically represented in Fig. 1.

2 Experimental

2.1 Materials

Kraft lignin (KL) (Sigma-Aldrich), 3-chloro-2-hydroxy-1-propansulfonic acid sodium salt hydrate (CHPSS) 95% (Sigma-Aldrich), glycidyl trimethylammonium chloride (GTMAC) ≥90% (Sigma-Aldrich), and chitosan with a medium molecular weight of 190000–310000 g mol^{-1} and 75–85% deacetylation (Sigma-Aldrich) were used as received. L(+)-lactic acid 95% (Acros Organics), sodium hydroxide (NaOH) (VWR chemicals), and deuterated water (D_2O) (VWR chemicals) were used as received. hydrochloric acid (HCl) solution (1 M) was also used. The dialysis membrane (MWCO: 500–1000 g mol^{-1}) was bought from Spectrum Labs. Nitrate salts of cobalt, copper, cadmium, nickel, lead, zinc, and chromium oxide were purchased from Sigma-Aldrich. Eriochrome Black T (EBT) was purchased from Acros Organics, while methyl orange (MO), methylene Blue (MB) hydrate, rhodamine B (RhB), and bovine serum albumin (BSA) were purchased from Sigma-Aldrich. Water spiked with PFAS agents perfluorobutane sulfonic acid (PFBS), perfluorohexane sulphonate (PFHxS), perfluorooctane sulfonic acid (PFOS), perfluorooctanoic acid (PFOA), and perfluorohexanoic acid (PFHxA) (total concentration 50 mg L^{-1}) was procured from IVL Svenska Miljöinstitutet, Stockholm. Two samples of wastewater from a mining area in Skellefteå in Sweden were kindly provided by Boliden AB. If not otherwise stated, deionized water from Merck Millipore was used.

2.2 Methods

2.2.1 Synthesis of ZL. The one-pot process of zwitterionic modification of lignin was developed from the process described in Guo *et al.*[18] Different reagent ratios were used for screening; the parameter settings found to provide the best results are reported here. First, 1 g KL and 0.15 mL of 2 M NaOH were mixed in 30 mL of water in a 100 mL round-bottom flask at 80 °C. CHPSS (0.3 g) and GTMAC (0.4 g) were dissolved in 10 mL of water each and sequentially added dropwise to the lignin mixture and left for 4 h under stirring. The colloidal solution was cooled to room temperature and neutralized with HCl to pH 7. Unreacted reagents and salt were removed by dialysis (3–4 days) against water, and then dried at 60 °C. The synthesis was repeated several times to validate the reproducibility.

2.2.2 Synthesis of ZLC. KL (2 g), chitosan (1 wt%), and 10 mL of water were mixed for 4 h at 50 °C. The mixture was further heated to 65 °C, and CHPSS, GTMAC, and NaOH were then added, keeping the same proportions as above. The suspension was stirred for 4 h, cooled to room temperature, neutralized to pH 7 if needed, and then centrifuged and washed repeatedly with water.

The as-synthesized materials of ZL and ZLC were purified by dialysis and washing by centrifugation, respectively, and were kept at 60 °C overnight to dry. Large granular materials were obtained for ZLC, which were further crushed by mortar and pestle to get uniform powder material that can be used as adsorbent media.

2.2.3 Batch adsorption studies and adsorption isotherms. Stock solutions (1 mg mL^{-1} water) of dyes (MO, RhB, MB and EBT) and metals (CrO_3, $Cu(NO_3)_2$, $Co(NO_3)_2$, $Cd(NO_3)_2$, $Ni(NO_3)_2$, $Pb(NO_3)_2$, $Zn(NO_3)_2$) were prepared by dissolution. In a typical batch adsorption experiment, 25 mg of ZL/ZLC was shaken with 25 mL of dye/metal spiked water, shaken (200 rpm) at room temperature. The water sample was collected to measure the leftover dye or metal concentration in treated water, using a UV-vis spectrophotometer or inductively coupled plasma optical emission spectrometry (ICPOES), respectively, and compared with the accuracy of three replicates ($n = 3$). The kinetics of the dye/metal adsorption was followed by withdrawing 1 mL of the treated solutions at different times and analysing the aliquots.

For isotherm determination, ZL/ZLC (25 mg) was immersed in 25 mL of metal-spiked water with the concentrations 1, 5, 10, 25, 50, 75, and 100 mg L^{-1} at pH 5.5, and shaken (200 rpm) at room temperature for 24 h. Then, aliquots were collected from the treated water and analyzed with UV-vis/ICPOES to determine the remaining concentration of the spiked entities. The equations involved in quantifying adsorbed amounts are given in the SI.

Kinetics of BSA adsorption over ZL/ZLC was measured using Pierce™ Bradford Protein assay kit by ThermoScientific.[19]

Performance was quantified using ICP-OES, UV-Vis, and LC-MS/MS; characterization techniques such as SEM-EDS, mapping, XRD, FT-IR, and XPS were carried out on the materials for a qualitative study of the adsorption phenomena.

2.2.4 Regeneration of ZLC. After each adsorption cycle where 50 mg of ZLC or ZL was soaked in 50 mL of 10 ppm Cr(VI)/Cu(II) mix solution, the treated water aliquot was collected for residual metal quantification, followed by soaking the treated adsorbent in 1 N HCl while shaking at 200 rpm for 4 h. Then the regenerated adsorbent was soaked in DI water for 2 h before subjecting it to another adsorption cycle of metals.

2.2.5 Protein adsorption. ZL/ZLC (50 mg) was soaked in 50 mL of a 250 mg L^{-1} input concentration of BSA in PBS buffer for 0–180 min under constant stirring of 200 rpm, and aliquots were collected at various time intervals.

2.3 Instrumentation

2.3.1 Fourier transform infrared spectroscopy (FT-IR). The FTIR spectra were obtained with the PerkinElmer Spectrum 100

FT-IR Spectrometer equipped with an attenuated total reflectance crystal. Each spectrum is the average of 16 accumulated scans with 4 cm^{-1} resolution. Baseline correction was done on all spectra using PerkinElmer Spectrum software V10.5.1.

2.3.2 Ultraviolet-visible spectroscopy (UV-vis). Absorbance measurements were carried out on a Shimadzu UV-2550 UV–vis spectrophotometer and recorded between 200 and 700 nm.

2.3.3 Inductively coupled plasma-optical emission spectroscopy (ICP-OES). ICP-OES was used to determine the absolute quantities of metal ions on ThermoScientific iCAP 6500.

2.3.4 ^{1}H-nuclear magnetic resonance spectroscopy (NMR). Spectra were obtained on a Bruker NMR spectrometer (400 MHz) at room temperature and recorded by the Bruker software. The samples were dissolved in D_2O with a concentration of about 20 mg mL^{-1}. Spectra were processed with MestReNova software.

2.3.5 Zeta potential (ZP). ZP was measured with malvern zetasizer pro. The samples were dissolved in deionized water, with a concentration of approximately 2 mg mL^{-1}, and triplicate measurements were taken to obtain the mean value *via* the ZS Xplorer software.

2.3.6 Thermogravimetric analysis (TGA). A Mettler Toledo TGA/DSC 1 Star system was utilized to conduct TGA, with samples of approximately 5–6 mg evaluated within a temperature range of 30–600 °C. A heating rate of 10 °C min^{-1} was employed in a nitrogen atmosphere with a 50 mL min^{-1} gas flow rate. The data was analyzed using the Mettler Toledo STARe V15.00b software.

2.3.7 Rheology. The shear stress rate was determined by rheological analysis with a TA Instrument model DHR-2. About 20 mL of each sample was used for the tests. The viscosity was recorded using a parallel plate of Peltier steel (25 mm diameter) with a gap of 300 μm.

2.3.8 Scanning electron microscopy (SEM). A Hitachi S-4800 Field-emission SEM was used for imaging. Before analysis, the samples were Pd/Pt sputter-coated (Cressington sputter coater) for about 2 min. The images were taken at working distances of 8.8 mm and 13.3 mm, with an acceleration voltage of 1000 V.

2.3.9 X-ray photoelectron spectroscopy (XPS). The oxidation states of the composite constituents and the presence of adsorbed metals were determined through XPS analysis. The XPS spectra were recorded on a Kratos AXIS Supra + XPS. ESCApe software was used for data acquisition and processing.

2.3.10 High-performance liquid chromatography-mass spectrometry (LC/MS-MS). PFAS concentrations in spiked water before and after batch adsorption experiments were quantified by LC/MS-MS at Research Institutes of Sweden (RISE), Borås, Sweden.

2.3.11 Powder X-ray diffraction (pXRD). pXRD was performed using a D8 Discover X-ray Powder Diffractometer from Bruker. Scans were performed in the 2θ range from 5 to 90°, for 30 minutes.

2.3.12 Energy-dispersive X-ray spectroscopy (EDS). Elemental mapping of the materials was done using a Hitachi TM3000, Tabletop Microscope (Hitachi Ltd, Japan). Samples were coated with a thin layer of gold and analyzed at an accelerating voltage of 5 and 15 kV in both secondary electron and back-scattered electron modes.

3 Results and discussion

3.1 Characterization of ZL and ZLC

Lignin was functionalized with zwitterionic moieties and combined with chitosan in a one-pot water-based process to achieve a granular and semi-porous biocomposite. Samples were first characterized using ^{1}H NMR spectroscopy to confirm the success of the reaction. In the set of ^{1}H NMR spectra shown in Fig. S1 (SI), the new peak appearing at 4.43 ppm (e') in the spectrum of ZL belongs to the protons of methine (–CH_2-CH(OH)–) of the attached GTMAC, while peaks at 4.25 ppm (b) and 3.66 ppm (a) correspond to methine and methylene groups of attached CHPSS, respectively. The intense signals for methyl protons from the $(CH_3)_3N$+ group observed at 3.12 ppm (g) from GTMAC overlap with those of (c) methylene protons of CHPSS in the ZL spectrum. The peaks at 3.82 ppm (d) of methylene oxirane of GTMAC, still appearing in the ZL spectrum with weaker intensity, indicate the presence of some unreacted GTMAC in the product. Overall, the appearance of the aforementioned peaks along with 4.17 ppm (a') belonging to CHPSS methylene attached to the aromatic hydroxy group of lignin and typical GTMAC peaks at 2.96 ppm (f') confirm the successful sulfonation and quaternization of lignin simultaneously, giving rise to the zwitterion-type functionalization. Characteristic features of chitosan at 4.8 ppm appear next to D_2O in the ZLC spectrum (Fig. S2, SI), while small peaks at 3.92–3.57 ppm overlap with KL, CHPSS, and GTMAC peaks. Furthermore, a peak at 1.99 ppm from chitosan shows its tiny presence in the spectrum of the ZLC composite.

ZL became a soft, fluffy material upon drying and yielded to the water pressure during batch adsorption tests. Therefore, ZL was deemed unfit for real-time water treatment applications, despite being a functional material. At the same time, ZLC was obtained as large and strong granules, which were further crushed by mortar and pestle to get a uniform powder material applicable as an adsorbent. The photographic images of ZL, ZLC granules, and powdered ZLC are provided in dried form in Fig. S3 (SI). ZLC is largely amorphous, as shown by *p*-XRD data. Fig. S4 (SI) shows XRD pattern (I) having two diffraction peaks at about $2\theta = 10.7°$ and 20.6° that are attributed to the hydrated crystal structure and amorphous region of chitosan. II shows a typical broad peak of lignin between $2\theta = 20$–23°, indicating its amorphous nature, which is wider in case of ZL (III), after functionalization of lignin. Pattern IV of the ZLC composite show a weaker and wider peak around $2\theta = 28°$, which shows that the chitosan has changed into an amorphous state after being combined with lignin. ZL and ZLC were imaged with SEM, as shown in Fig. 2a and c. It was observed that ZLC, being a composite with chitosan, showed higher aggregation and formed almost 10 times larger particles, while ZL was finer. While the parent lignin powder showed porous near-spherical structures with visible cracks and openings (Fig. 1), the composite showed entirely different morphology of irregular-shaped granular structures, resulting in particle sizes in the

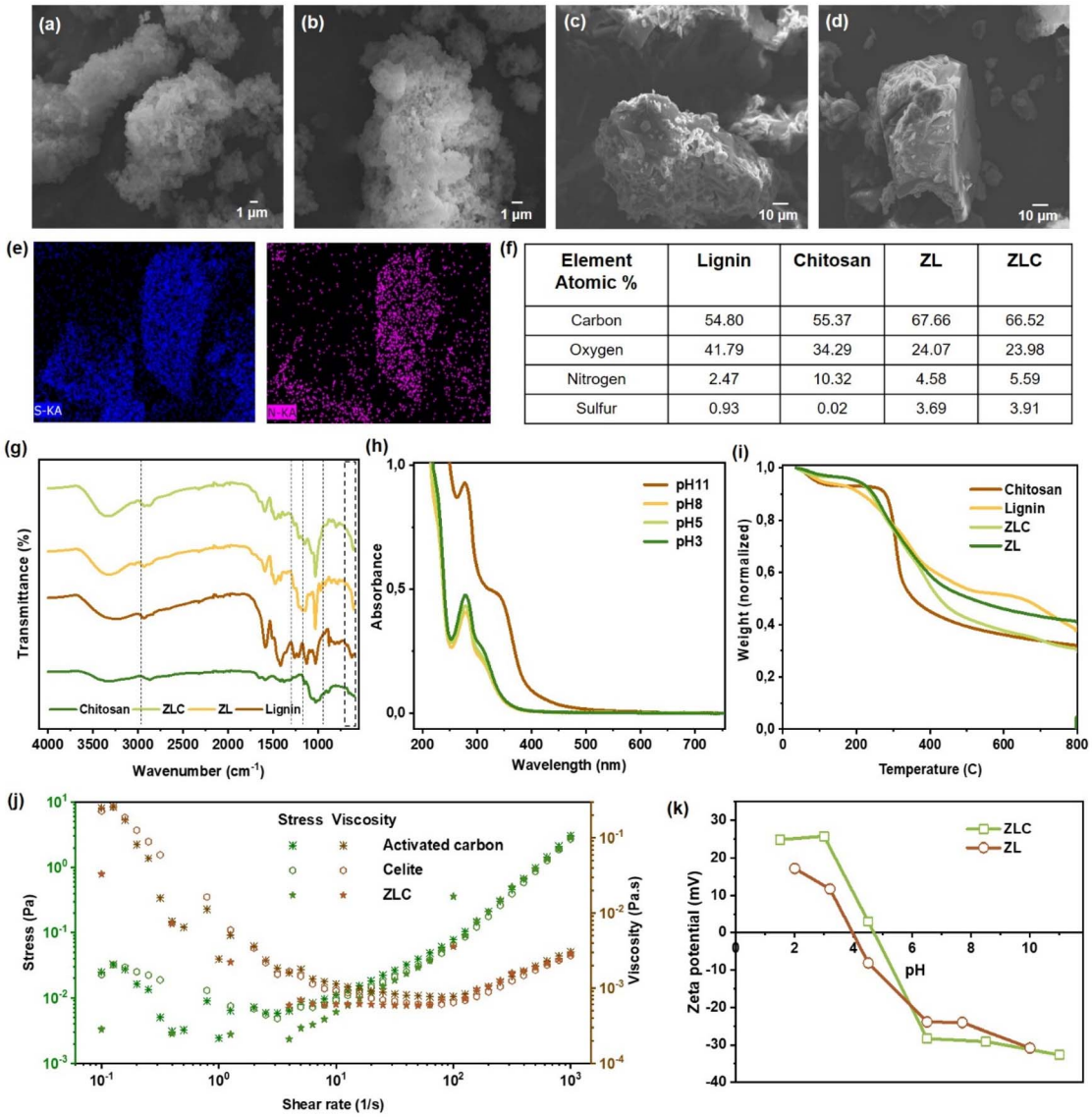

Element Atomic %	Lignin	Chitosan	ZL	ZLC
Carbon	54.80	55.37	67.66	66.52
Oxygen	41.79	34.29	24.07	23.98
Nitrogen	2.47	10.32	4.58	5.59
Sulfur	0.93	0.02	3.69	3.91

Fig. 2 Characterization of ZL and ZLC: SEM images of ZL (a), (b) and ZLC (c), (d) before and after adsorption, respectively; (e) elemental mapping of N and S in ZLC; (f) elemental composition of ZL and ZLC by EDS; (g) FT-IR spectra of lignin, ZL, ZLC and chitosan; (h) UV-vis spectra showing chemical stability of ZLC at various pH; (i) thermal behavior of lignin, ZL, ZLC and chitosan; (j) rheological properties of ZLC compared with commercial Celite and Activated carbon; (k) zeta potential of ZLC and ZL in the pH range of 1–11.

range of 20–100 μm for ZLC and 5–20 μm for ZL. Surface morphology of ZLC cross-section at higher magnification is shown by SEM images in Fig. S5 (SI). Specific surface area (SSA) and pore volume were determined for the lignin precursor and ZLC using BET N_2 adsorption. SSA and pore volume of lignin were 0.60 $m^2\ g^{-1}$ and 3.4 × 10^{-3} $cm^3\ g^{-1}$, respectively, while that of ZLC was 1.86 $m^2\ g^{-1}$ and 7.8 × 10^{-3} $cm^3\ g^{-1}$, respectively. Although composite formation increased the SSA and porosity by 2–3 times compared to the precursor, the values are still lower than those of nanomaterial-based adsorbents like MOFs, metal oxides, or carbon-based adsorbents like biochar, activated carbon *etc.*; indicating the zwitterionic functionalization of ZLC playing the major role in defining the uptake capacity of ZLC. No change in particle morphology was observed upon exposure to various pollutant concentrated solutions, which implies that adsorption is the mode of interaction (Fig. 2b and d). The absence of a drastic change in particle size indicates that ZLC does not disintegrate upon agitation and that the composite remains stable in water. EDS analysis (Fig. 2f) indicates that both the precursor and resulting materials are primarily composed of carbon, followed by oxygen. Notably, the nitrogen and sulfur content increased after zwitterionic modification of lignin with NH_4^+ and SO_3^- functional groups in ZL and ZLC, as further illustrated in the elemental mapping (Fig. 2e).

The FT-IR spectra of the precursor and the product materials are shown in Fig. 2g. Sharpening of O–H peaks in the 3500–3000 cm^{-1} region of ZLC and ZL compared to that of lignin and chitosan imply reduction in H-bonding due to bonding/substitution with other functional groups. Aside from the

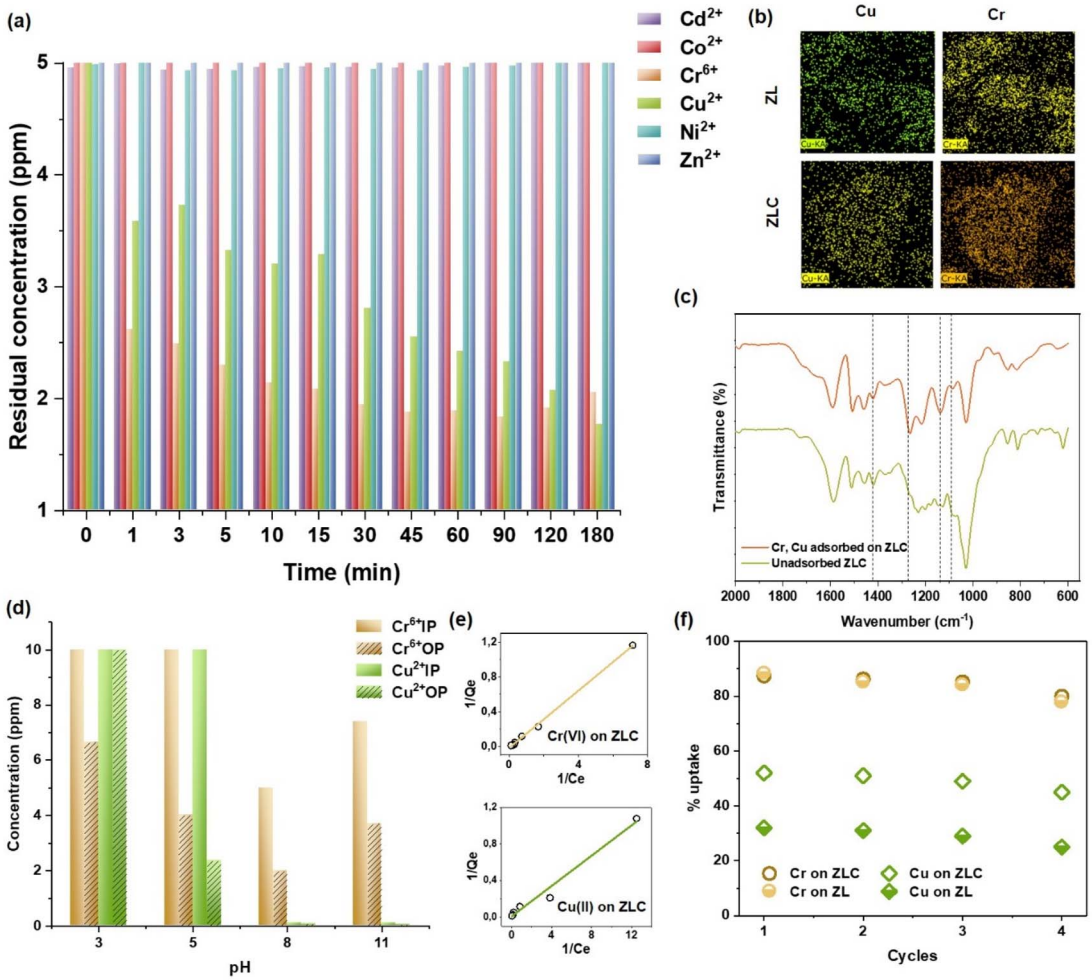

Fig. 3 Heavy metal adsorption on ZLC: (a) adsorption kinetics of ZLC tested against various heavy metal ions between 0–180 min; (b) elemental mapping of ZL and ZLC surface after Cu(II) and Cr(VI) adsorption; (c) FT-IR spectra of ZLC before and after adsorption; (d) concentration of Cr(VI) and Cu(II) in the samples before (IP) and after (OP) treatment with ZLC at pH 3, 5, 8, and 11; (e) Langmuir isotherm showing Cr(VI) and Cu(II) uptake capacity; (f) number of cycles for Cu(II) and Cr(VI) adsorption after adsorbent regeneration.

characteristic peaks contributed by lignin and chitosan, ZL and ZLC spectra show extra bands at 1145 and 1345 cm^{-1} corresponding to S=O stretching coming from R–SO_3^- addition by CHPSS, shown by dotted lines. The C–N stretch of the quaternary ammonium found at around 1475 cm^{-1}, C–$N(CH_3)_3^+$ symmetric stretch bands between 950–800 cm^{-1}, and 3040 cm^{-1} for C–H stretch of +NCH_3,[20] were all coming from the quaternary ammonium functional group incorporated from GTMAC. The chemical stability of ZLC was assessed in the pH range of 3 to 11 (Fig. 2h), and no disintegration over the acidic to the basic range was detected; however, in the extreme alkaline region (pH ≥ 11), lignin may start isolating itself from the composite. The thermal decomposition behaviour is not significantly affected by the chemical modification. Chitosan undergoes major degradation around 270 °C, which is associated with the depolymerization of the polysaccharide backbone, dehydration of saccharide rings, and decomposition of acetylated units. Lignin, on the other hand, shows significant weight loss at approximately 190 °C, due to degradation of its polyphenolic backbone and cleavage of weak ether and ester linkages. In ZLC, the observed T_{max} of 230 °C indicates a shift in the thermal stability compared to the individual components, suggesting interactions between chitosan and lignin during thermal decomposition. Furthermore, differences in the char residue were evident. Lignin typically leaves a higher char yield due to its aromatic structure, which favors carbonaceous residue formation. Chitosan, in contrast, produces less char because of its relatively linear polysaccharide backbone and lower aromatic content. ZLC displayed an intermediate char residue, implying partial stabilization of chitosan by the aromatic framework in lignin (Fig. 2i). High mechanical strength and robustness is crucial for an adsorbent to be used in a filter module and able to withstand the water flux and for avoiding pressure drop in the column filter by clogging. Hence, ZLC was analyzed for rheological properties and compared to commercial benchmark materials such as activated carbon and Celite (Fig. 2j). Both the shear stress–shear rate curve and the viscosity–shear rate curve of ZLC follow closely the behavior and values of commercial activated carbon and celite (kieselguhr) with a distinct non-Newtonian behavior. In the process of

adsorption, the overall surface charge of the material plays a significant role in influencing electrostatic interactions with various charged contaminants in water. Hence, pH-dependent zeta potential was recorded for ZL and ZLC dispersed in water (0.05 wt%) in the pH range of 1–11, shown in Fig. 2k. Isoelectric points of ZL and ZLC appeared at pH 4 and 4.7, respectively. ZLC showed higher dispersion stability than ZL at low and high pH regions.

3.2 Adsorption of heavy metals

3.2.1 Adsorption kinetics, characterization and isotherm. ZL and ZLC were subjected to a water sample spiked with a mixture of the heavy metals Cd(II), Co(II), Cr(VI), Cu(II), Ni(II), and Zn(II) at a concentration of 10 mg L^{-1} each. The residual concentrations after adsorption were measured by ICP-OES. Both ZL and ZLC showed an affinity towards Cr(VI) and Cu(II) and could remove up to 90% from water. Upon studying the adsorption kinetics of ZLC, it became clear that Cr(VI) and Cu(II) adsorb onto its surface at different rates (Fig. 3a) while the other metal ions do not show any significant reduction over time. The time-resolved data were modeled using pseudo-first and pseudo-second order kinetic models. Based on the value of R^2, it was clear that for all adsorbates used in this work, the pseudo-second order model fitted the experimental data better (Table S1, SI). A pseudo-second order kinetics model assumes that the adsorption rate is influenced by adsorbent–adsorbate interactions.[21] To further understand the adsorption mechanism, the intraparticle diffusion model was applied to identify the rate-limiting steps between surface adsorption and diffusion into the pores, discussed in Fig. S6 (SI). Fig. 3b shows the distribution of Cr and Cu ions over the surface of ZLC and ZL in a uniform fashion as visualized by elemental mapping. After adsorption, saturated ZL and ZLC were subjected to pXRD (Fig. S7, SI), the broad peak at $2\theta = 15$–$30°$ in patterns II and IV suggest no changes to the amorphous structure, confirming adsorption does not cause any structural changes to the adsorbents. The broad hump at $2\theta = 38$–$45°$ in patterns II and IV is an overlap of metal oxide features of CrO_3/Cr_2O_3 (common characteristic peak at 43.9°) and CuO/Cu_2O (characteristic peak CuO at 38.9° and Cu_2O at 42.3°) adsorbed on ZL and ZLC, which is absent in the pristine adsorbents (I and III). FT-IR spectra of ZLC before and after metal adsorption are shown in Fig. 3c. ZLC shows characteristic peaks related to the $-SO_3^-$ group at 1090, 1175, and 1126 cm^{-1} due to S=O stretching, symmetric and asymmetric stretch of S–O groups alongside a band at 1420 cm^{-1} due to –OH bending, which either diminishes or vanishes in the metal-adsorbed ZLC. Also, weak bands at 918 and 968 cm^{-1} stemming from $+N(Me)_3$ of ZLC cannot be seen in the metal-loaded ZLC, which suggest that these are the N- and S-active sites participating in metal adsorption, whereas new peaks at 908 and 1138 cm^{-1} can be attributed to Cr and Cu ion adsorption.[22,23] To improve the adsorption efficiency, it is interesting to explore the pH range where ZLC performs best. pH-dependent adsorption experiments showed that maximum Cr(VI) and Cu(II) adsorption occurred at pH 5 (Fig. 3d). Alkaline pH promotes precipitation of the dissolved metal salts in the input water samples, thus making it an unsuitable condition to work in. Fig. 3e represents the Langmuir isotherm plots for the adsorption of heavy metals and dyes on ZLC to observe its maximum uptake capacity for each contaminant. The isotherm data were also modeled for the Freundlich isotherm, and both models were applied to ZL as well to compare the uptake capacities (Table 1). Langmuir isotherm showed higher R^2 values in every case; linear fits are shown in Fig. S8 (SI).

3.2.2 Reusability. To study the reusability of the materials, ZLC and ZL were tested for four cycles of adsorption of metals with acid regeneration after each cycle (Fig. 3f). It was observed that both ZLC and ZL maintained 80–90% removal of Cr(VI). For Cu(II), ZLC removed up to 60% and ZL up to 40% till the fourth cycle. The difference between the removal of the two metals may be due to competitive adsorption on the active sites between the two ions.

Although ZL was tested for heavy metals in initial experiments to check its functionality, it was not further used for organic dyes and PFAS removal due to its soft and weak structure, that made it difficult to handle.

3.2.3 Testing real water samples. ZLC was further subjected to authentic wastewater matrices, sampled from effluents from a mining site in northern Sweden. Such effluents can be challenging to process, as they, alongside dissolved and suspended metalloids, may contain physical contaminants such as suspended solids and sediments, and natural organic matter

Table 1 Uptake capacities of ZL and ZLC towards various contaminants as per Langmuir and Freundlich isotherms

			Isotherm			
			Langmuir		Freundlich	
Sample no.	Effluent	Material	Uptake (mg g^{-1})	R^2 value	Uptake (mg g^{-1})	R^2 value
1	Cr(VI)	ZL	71.4	0.99	7.4	0.97
2	Cr(VI)	ZLC	108.6	0.99	6.8	0.99
3	Cu(II)	ZL	156.2	0.97	7.7	0.98
4	Cu(II)	ZLC	196.0	0.98	14.6	0.98
5	MB	ZLC	192.3	0.94	18.2	0.69
6	MO	ZLC	4166.6	0.90	40.7	0.77
7	RhB	ZLC	71.9	0.93	6.7	0.93
8	EBT	ZLC	1030.9	0.88	13.8	0.81

Table 2 Metal removal from real wastewater samples after adsorption by ZLC

Real water samples	pH	Cr(VI) removal	Cu(II) removal
Sample 1	8.1	62%	97%
Sample 2	8.3	63%	89%

that can cause fouling. Such effluents also vary in pH, depending on contents and seasonal fluctuations. The collected mining effluents, Sample 1 and Sample 2, were analyzed to determine the physicochemical parameters and level of concentration of metals of interest, which were found to be low (Table S2, SI). Hence, they were spiked with 20 ppm each of Cr(VI) and Cu(II). Performance of ZLC for metal removal is provided in Table 2.

3.2.4 Adsorption mechanism by XPS analysis. The components of ZLC and their interaction with metals were also studied by X-ray photoelectron spectroscopy (XPS), as shown by the survey spectra in Fig. 4a. The survey spectrum of ZLC before adsorption shows the N 1s feature with higher intensity than S 2p, indicating the zwitterionic functional groups. After adsorption, Cr 2p appears with higher intensity than Cu 2p in ZLC. The metal ion peaks correspond to the uptake during batch studies and were expanded and plotted as shown in Fig. 4b to better understand the peak components. While ZLC before adsorption shows no heavy metal features, ZLC after adsorption shows clear peaks of Cr 2p 3/2and Cr 2p 3/2 at 587.1 and 577.3 eV, respectively, indicating Cr(III) species in hydroxide/oxide form, which can be attributed to reduction. In addition, the small peak at 573.2 eV also shows traces of metallic Cr. For Cu(II), Cu 2p 1/2and Cu 2p 3/2 at 952.9 and 933.1 eV, respectively, the XPS spectrum clearly shows reduction, as demonstrated by the absence of a satellite peak at around ~943 eV. To analyze the mechanism of adsorption, the active sites of SO_3^- and $-N(CH_3)_3^+$ were focused and S 2p and N 1 s spectra were deconvoluted to get their different binding states. The S 2p feature of pristine ZLC in Fig. 4c shows two

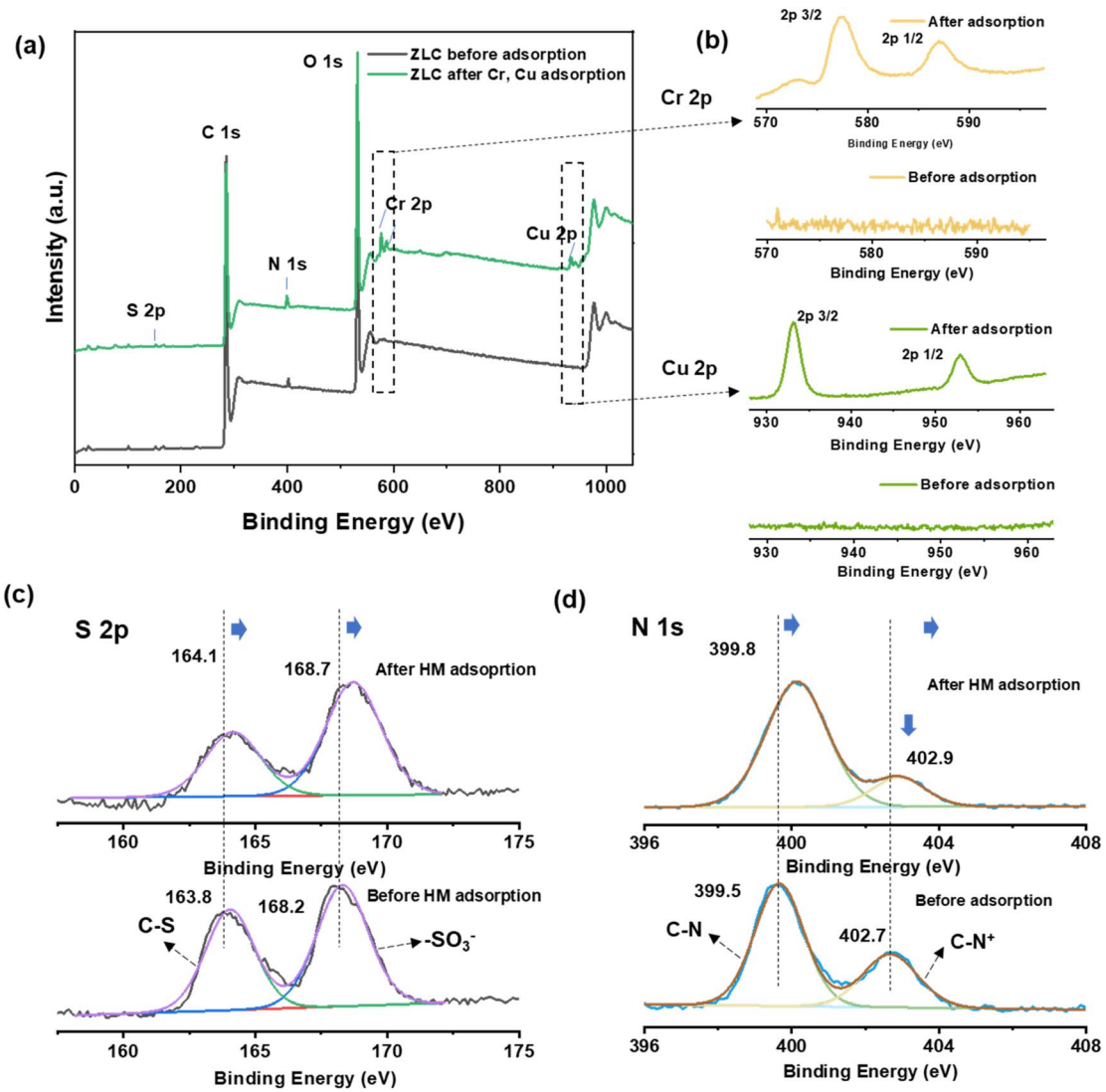

Fig. 4 XPS survey spectra of (a) ZLC before (black) and after (green) Cu and Cr adsorption; (b) the Cr 2p and Cu 2p regions features on the survey spectra are expanded; (c) deconvoluted XPS spectra of S 2p and N 1s regions of ZLC before and after metal adsorption.

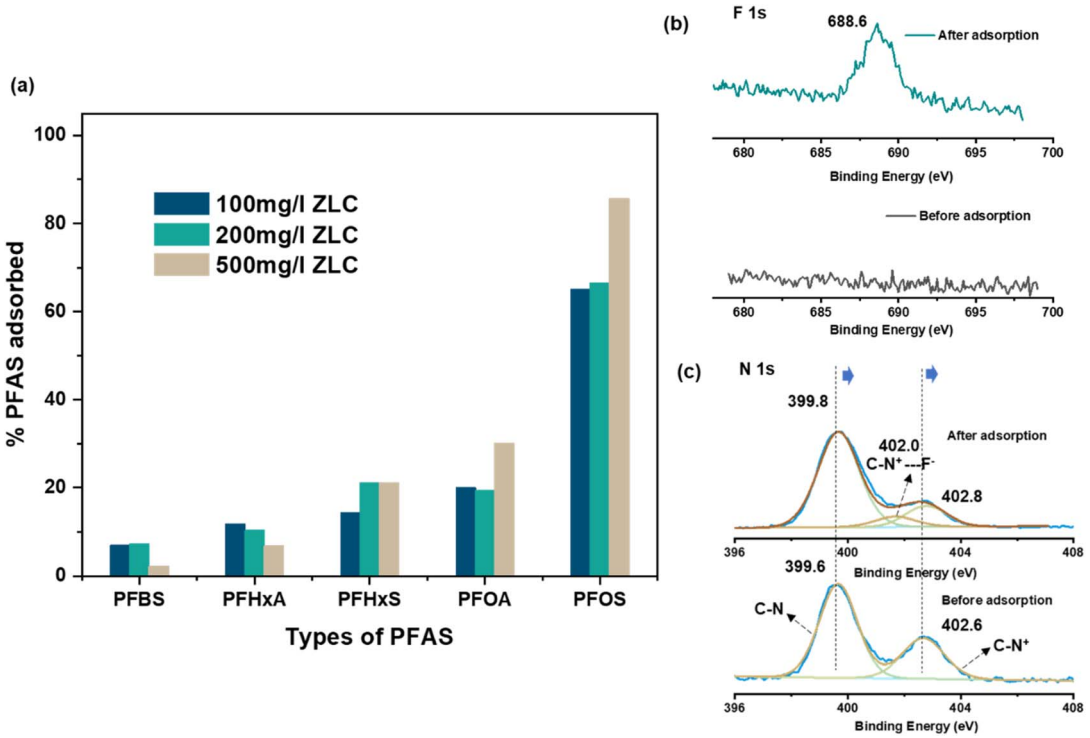

Fig. 5 (a) Adsorption performance of ZLC tested against five different PFAS species; (b) XPS survey spectra showing F 1 s feature on ZLC after PFAS adsorption; (c) deconvoluted XPS spectra of N 1s regions of ZLC before and after PFAS adsorption.

components at 163.8 and 168.0 eV, respectively, corresponding to C–S and SO_3^- bonds.[15,24] They shift to 164.1 and 168.7 eV after adsorption, and the larger shift in SO_3^- binding energy indicates its direct interaction with Cu(II) cations during the adsorption process. In the case of the N 1 s peak (Fig. 4d) in pristine ZLC, two components appear at 399.5 and 402.7 eV, attributed to N–C and +N–C bonds of the quaternary ammonium group, which are observed to shift to 399.8 and 402.9 eV. The equilibria of Cr(VI) in water are very complex.[25] The observed shift in the N 1s peak can be due to Cr(VI) anionic species, chromate $H(CrO_4)^-$ or $(Cr_2O_7)^{2-}$ in water (pH range 5–6.5), interacting with the +N- center of the group. The intensity of the +N–C component decreases upon metal adsorption, which can be attributed to the N+ site strongly interacting or coordinating with the negative charges of the chromate ion.

3.3 Adsorption of organic contaminants: PFAS

3.3.1 Performance of ZLC. To check the ability of ZLC to scavenge PFAS molecules from water, ZLC dosages of 100, 200, and 500 mg L^{-1} were exposed to a water sample containing a mixture of PFAS molecules with different chain lengths, namely PFBS, PFHxA, PFHxS, PFOA, and PFOS, in an unadjusted pH 5–6 range of the medium. The stock solution of PFAS compounds was prepared at a concentration of 50 μg L^{-1} for each substance, which is considerably higher than the levels typically found in drinking water. This elevated concentration was not intended to simulate a drinking water scenario but rather to represent a highly contaminated site requiring remediation. Additionally, the use of a higher concentration ensured that the purified water remained well above the analytical detection limit, thereby increasing the reliability of the post-treatment measurements. After a contact time of 24 h, the adsorbent was separated, and the water sample was analyzed using LC-MS/MS to measure the remaining PFAS concentration. ZLC performed better in removing longer-chain PFAS molecules, especially PFOS, that showed 80–90% removal (Fig. 5a). Corresponding LC-MS/MS graphs are provided in Fig. S9 (SI).

3.3.2 Adsorption mechanism. The PFAS-loaded ZLC was analyzed using XPS to reveal the interaction between the contaminants and the adsorbent. Fig. 5b shows that F 1s clearly appeared in the survey spectra of PFAS-adsorbed ZLC at 688.6 eV. The tested PFAS compounds were mainly negatively charged, so the molecules essentially existed in water as SO_3^- or CO_2^- entities that interacted with the quaternary ammonium active sites of ZLC during adsorption. The shift and changes in the N 1s components upon adsorption can be seen in Fig. 5c. The peaks were slightly shifted to higher binding energies, accompanied by a sharp decrease in the intensity of +N–C component. A new component emerges at 402.0 eV due to F- of PFAS molecules binding with +N–C functionality of ZLC, suggesting complexation. Relatively higher uptake of long chain PFAS molecules also indicates hydrophobic interactions with lignin's aromatic rings in ZLC. The molecules may show competitive adsorption, and the experimental results do not reveal the uptake capacity for each kind of PFAS molecule individually. That could be obtained by testing ZLC for each PFAS species separately as experiments in future work. Also, it would be interesting to see the performance of ZLC towards positively charged and zwitterionic PFAS molecules.

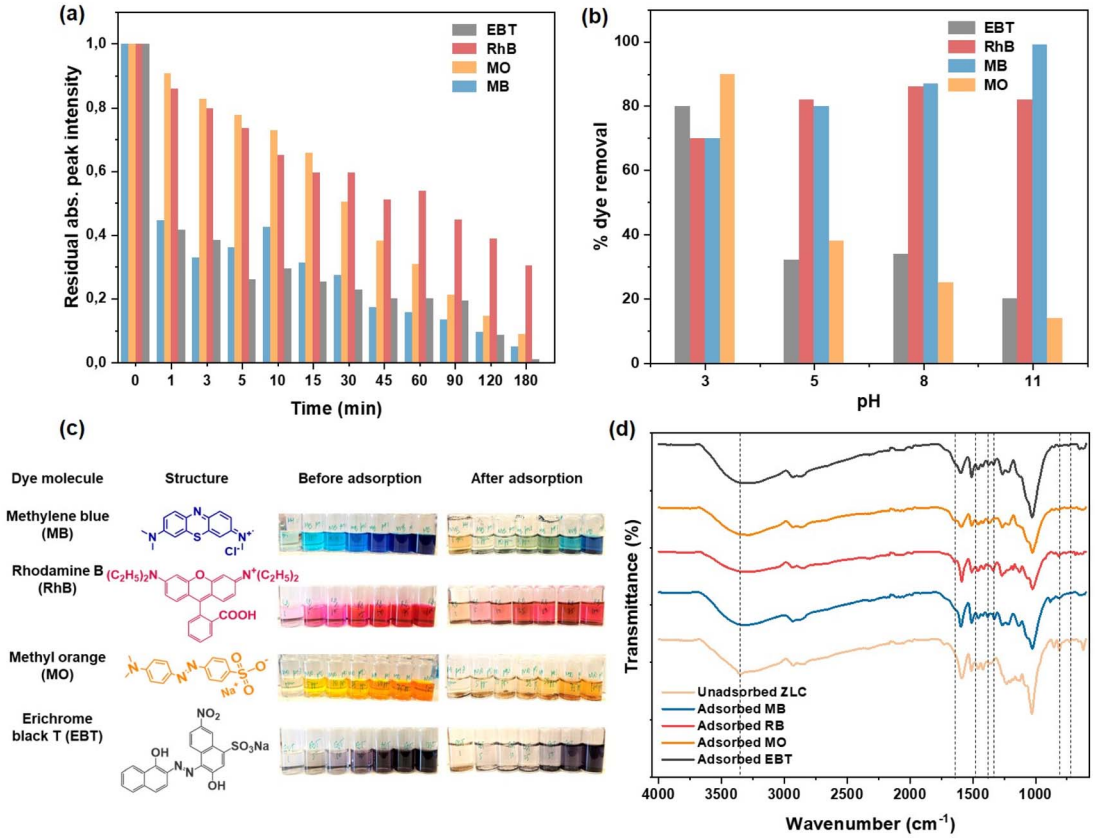

Fig. 6 Adsorption of organic dyes on ZLC: (a) time and (b) pH-dependent adsorption of EBT, RhB, MO and MB; (c) photographs showing the concentration (1, 5, 10, 25, 50, 75 and 100 ppm) dependent colors of the dyes before and after adsorption, including chemical structures of the tested dyes; (d) FT-IR spectra of ZLC before and after adsorption of each dye.

3.4 Adsorption of organic contaminants: cationic and anionic dyes

3.4.1 Performance of ZLC. The aromatic dyes MB and RhB are cationic, while MO and EBT are anionic in nature. In view of the zwitterion-type functionalization of lignin composite, both kinds of dyes were tested, and ZLC showed very high removal efficacy towards all, verifying the versatility of the zwitterionic functionalization of the lignin biocomposites. Time-dependent adsorption was carried out from 0–180 min for each dye separately (Fig. 6a). The tested dyes show different rates of adsorption during the time range, as evident from the residual peak intensities in the absorbance spectra, plotted against time. Their kinetic behavior was modeled, and a pseudo-second order relationship gave the best fit (Table S1, SI). Dyes in wastewater exist in a wide range of pH, so to study the influence of pH on dye removal, adsorption experiments were carried out in the pH range of 3–11. Removal of the anionic dyes increased as the pH decreased into the acidic region (Fig. 6b). This is because ZLC would show maximum positive surface charge in acidic pH by attracting maximum H^+ ions from the medium, which would electrostatically attract the anionic dye molecules. It is validated by the zeta potential measurement of ZLC as a function of pH (Fig. 2k). The opposite was observed for MB, which is a cationic dye, where removal was the highest at alkaline pH. RhB is rarely influenced by the pH change because of its ability to exist in cationic or zwitterionic forms as pH changes from acidic to basic. The chemical structures and optical images showing the removal of each dye as a function of dosage can be seen in Fig. 6c. Isotherm experiments were carried out for each dye, and data were fitted with Langmuir and Freundlich models. The maximum uptake capacities are listed in Table 1, and their linear fits are shown in Fig. S10 (SI). The Langmuir isotherm model gave higher R^2 values and a very high uptake for the dyes. ZLC exhibited uptake capacities as high as 4166.6 and 1030.9 mg g^{-1} for MO and EBT, respectively, and 192.3 and 71.9 mg g^{-1} for MB and RhB, respectively. These values indicate that ZLC showed higher adsorption efficiency towards anionic dyes. Also, comparatively lower R^2 values may suggest that the dyes may follow other forms of monolayer or multilayer adsorption models.

3.4.2 Adsorption mechanism. Higher uptake of dyes can also be partially due to other intermolecular adsorbent–adsorbate interactions such as π–π stacking and hydrogen bonding due to the complex chemical structure of the lignin-based composite and organic molecules.[26] Saturated ZLC after each dye adsorption was subjected to FT-IR spectroscopy to study the qualitative changes in their chemical structures. FT-IR spectra of ZLC before and after adsorption of dyes are shown in Fig. 6d. To facilitate peak identification, spectra were also recorded for each dye in the dry state. (Fig. S11–S14, SI). The absorption band around 3400 cm^{-1} in the pristine ZLC, logically assigned to O–H

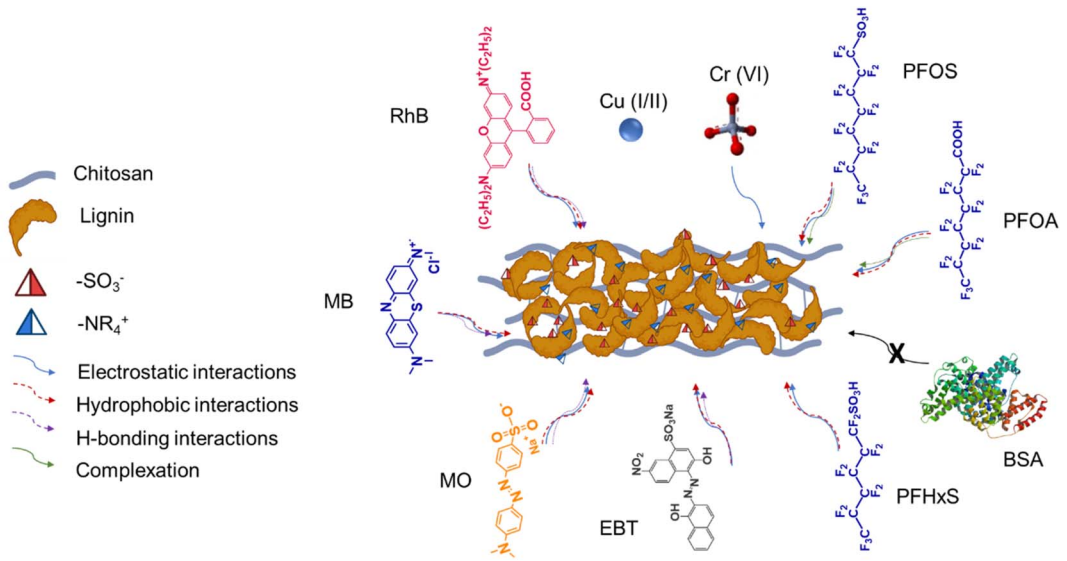

Fig. 7 Molecular interactions between the contaminants and ZLC leading to adsorption.

stretching vibrations, appears to become broader in the adsorbed ZLC samples in general, due to absorption of water by the material during the adsorption process. More information about the adsorbed dye species on the material was obtained from the middle/lower frequency region of the spectra. For dye-adsorbed ZLC systems, new peaks emerged, and existing peaks changed due to adsorption. In case of MB adsorbed on ZLC, appearance of extra peaks at 1663 cm^{-1} (attributed to C=C and C=N vibrations in heterocyclic groups of MB), 1383 and 1328 cm^{-1} (due to C–N, C=S+ stretch of heterocycles), 1268 cm^{-1} for C–H bending, 884 cm^{-1} for dimers or H-aggregates, while 646 cm^{-1} for γ and δ (C–S–C) groups confirm the presence of adsorbed MB on the surface of ZLC.[27] In case of RhB adsorbed on ZLC, a peak at 1648 cm^{-1} for stretching vibrations of C=C and C=N groups of aromatic rings, 1340 and 1244 cm^{-1} for C–C and C–O–C stretching, and 683 cm^{-1} for aromatic C–H wagging vibrations confirm the presence of adsorbed RhB on the ZLC surface.[28,29] In the MO-adsorbed ZLC spectrum, weak bands appeared at 1649 and 1600 cm^{-1} attributed to N–H bending/C=C stretch and N=N stretching vibrations, respectively. Peaks at 1264 and 1215 cm^{-1} stemmed from C–N stretching of aliphatic amines, and a weak band at 814 cm^{-1} due to the 1,4-disubstituted (para) benzene ring confirmed the presence of the azo dye on ZLC surface.[30,31] Apart from the azo-related peaks at 1654 and 1597 cm^{-1}, peaks appearing at 1334 and 1215 cm^{-1} due to $-NO_2$ and $-SO_3$ groups, respectively, confirmed the EBT adsorption on the ZLC surface.[32]

A schematic representation summarizing various possible molecular interactions between ZLC and different contaminants for adsorption is provided as Fig. 7.

3.5 Protein fouling

Protein adsorption is a ubiquitous fouling process that can have undesirable consequences for any adsorbent operating in the field or with industrial effluents. Thus, ZL and ZLC were tested for their protein resistance by exposing them to a model protein (bovine serum albumin, BSA) at room temperature, and the adsorption process was analyzed in a time-dependent manner using the Pierce™ Bradford Protein assay. The percentage of BSA absorbed over time was calculated from the absorbance data (Fig. 8). It was observed that the BSA molecules initially interacted slightly with the ZLC surface, but no adsorption was observed beyond 60 min. This can be due to the positive and negative functional groups on ZL and ZLC surfaces, making the material very hydrophilic, and the electrostatic interactions among the groups can result in their reorientation towards the interface of the aqueous medium, giving rise to a hydration layer that can effectively promote protein resistance.[33]

3.6 Comparison with the literature

Several conventional and novel sorbents have been used for the removal of various contaminant species from aqueous solution

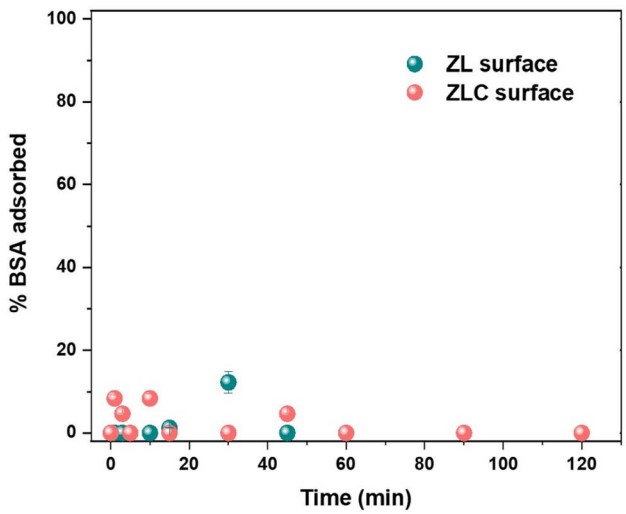

Fig. 8 Time-dependent performance of ZL and ZLC tested against adsorption of BSA using Pierce™ Bradford Protein assay method.

Table 3 Broad-spectrum water purification performance shown by various adsorbents

Adsorbent	Removal capacity (mg g^{-1} or %)			Antifouling properties	Reference
	Heavy metals	PFAS	Organics		
ZLC	71.4 Cr(VI), 156.2 Cu(II)	PFOS 86%, PFOA 30%	MB 192.3, MO 4166.6, RhB 71.9, EBT 1030.9	Yes	**This work**
Walnut shell activated carbon	51.3 Cr(VI), 204.1 Cu(II)	—	—	—	34
Sorghum bicolor	20.7 Cr(VI), 24.8 Cu(II)	—	—	—	35
Biosilica/Silk fibroin/ Polyurethane	201.56 Cr(VI), 31.69 Cu(II)	—	—	—	36
ZIF-67/BC/CH aerogel	152.1 Cr(VI), 200.6 Cu(II)	—	Active red X–3B ~100%	—	37
γFe2O3 NP@cellulose/ Activated carbon	—	—	MB 1.40(4.39×10^{-3} mmol g^{-1}), MO 2.12 (6.48×10^{-3} mmol g^{-1})	—	38
Chitosan grafted-benzaldehyde/ montmorillonite/algae	—	—	BG 899.5, RB19 213.6	—	39
MgO–SiO_2/lignin at 313 K	35.30 Cu(II), 69.42 Cd(II)	—	—	—	40
Carboxymethylated lignin/ Fe_3O_4	189.85 Pb(II), 124.43 Cu(II), 106.97 Ni(II)	—	—	—	41
Amino-functionalized lignin microspheres	74.84 Cd(II), 54.20 Cr(VI), 53.12 As(V), 49.42 Ni(II)	—	—	—	42
Quaternized lignin	—	—	RB 41.85, MB 49.47, AB-92 110.53, CR 134.61	Biocompatible	43
Fe_3O_4/C-ACLS carbon coated magnetic ferric oxide@calcium lignosulfonate (ACLS)	—	—	CR 198.8, TY 192.3, EBB-R 198.5	—	44
Lignin-based polyurethane foam	98.2 Cu(II)	—	MB 67.1, RhB 96.1	—	45
Iron anchored graphene (G-fe) nanosheets from dried seaweed (ulva fasciata)	645 Pb(II)	—	CR 970, CV 909, MO 664, MB 402	—	46
Cationic quaternized nanocellulose	—	PFOS 559, PFOA 405, PFBS 319, PFBA 121	—	—	47
Chitosan/F–COF	—	PFOS 8307.1, PFOA 6177.1, GenX 4603.3	—	—	48
Rice straw-derived biochar-ALG composite beads	—	PFOS ~99%, PFBS 40%	—	—	49
Reduced graphene oxide modified zinc ferrite immobilized chitosan beads (rGO-ZF@CB)	—	PFOA 16.07, PFOS 21.64	—	—	50
Silane-modified zirconium-based coagulant DZHC	94% Cu(II), 100% Pb(II), 99% Cr(VI), 32% Zn(II)	PFOS 100%, PFOA 99%, PFHxS 99%, PFHxA 96%, PFBS 98% and PFBA 85%	—	—	51
Modified coal fly ash (CFA)	—	PFDoDA 3.5, PFBA 1.8, PFHxA 1.8, PFOA 2.3, PFDA 3.0	—	—	52
Hardwood-derived biochar	Cd(II)	PFOS 16.1, PFOA 7.7, GenX 4.8	—	—	53
GAC	92% Cd(II), 81% Cu(II), 84% Pb(II), of 72% Ni(II) and 52% Zn(II)	PFOS/PFOA 4–5 mg mg^{-1}	Pharma molecules	TSS dependent	54
Zr-based porphyrinic MOF (PCN-224)	—	PFOS 963, PFHxS 517, PFBS 395	—	—	55

for broad-spectrum water purification. While, most of them show sensitivity towards one or two types of contaminant species, multifunctionality of ZLC can be clearly observed when compared with other adsorbents. These findings are summarized together with data from this work (Table 3).

Conventional materials such as activated carbon (GAC and PAC) dominate commercially due to their efficiency and cost-effectiveness, while ion exchange resins are expensive but known for their selective removal capacity. These materials come with high energy demands, frequent replacement needs, and CO_2 emissions. ZLC offers significant advantages over these

alternatives as it captures a wide range of contaminants, including PFAS, heavy metals, and dyes, across a broad pH range while resisting fouling. It is produced *via* a simple, green, water-based one-pot process at 70–80 °C, unlike activated carbon, which requires high-temperature activation (700–800 °C), and is often not regenerated due to low cost, causing untreated spent materials to end up in landfills. ZLC is mainly made from lignin and chitosan – easily available and inexpensive raw materials, making it cost-effective and it can be regenerated multiple times. It is thermally stable and chemically robust, with high mechanical stability (comparable to activated carbon and Celite shown in Fig. 2), thus making ZLC comparable to commercial filter materials. With further enhancement of its uptake capacity, its multifunctionality, ease of production, and reusability make it a scalable, sustainable alternative for industrial applications.

4 Conclusions

This study demonstrates the preparation and performance of a unique multifunctional composition that is capable of adsorbing anionic, cationic, and neutral chemically diverse contaminants effectively across a range of pH levels, while avoiding biofouling, making it a robust choice for real-world applications. Functionalized lignin with a structural reinforcement added by chitosan (ZLC) were prepared using a green, simple, and water-based one-pot synthetic procedure. Morphological characterization of the materials conveyed that they are micron-sized granulated, amorphous, mechanically and thermally stable, while chemically they are stable in a wide pH range. Lignin modified with sulphonyl and quaternary ammonium groups gives the composite a zwitterion-type functionalization that acts as active sites for adsorption. ZLC were tested as adsorbents and demonstrated excellent performance for an array of water contaminants such as Cr and Cu ions, PFAS molecules such as PFOS, and the synthetic dyes MB, MO, RhB, and EBT. The materials also performed well for real water samples from mining areas and are reusable for multiple cycles. The adsorption process was in each case studied using XPS and IR spectroscopy. XPS data confirmed the interaction of contaminants with the N and S active sites of the materials. Further, the adsorption process followed pseudo-second-order kinetics and Langmuir isotherm, which showed very high uptake capacities for the large number of contaminants. This sustainable, low-cost material presents a viable solution for improving broad-spectrum water purification systems worldwide, addressing the constraints of conventional treatment approaches.

Author contributions

S. M., conceptualization, methodology, data collection, investigation, writing-original draft, and editing; S. L., investigation, editing, and calculations; U. E., conceptualization, supervision, writing-review, editing, and acquired funding. All authors have read and agreed to the published version of the manuscript.

Conflicts of interest

There are no conflicts of interest to declare.

Data availability

Data generated or analysed during this study are included in this published article and its supplementary information (SI) . Supplementary information: includes figures and tables that provides formulae and equations; ^{1}H NMR and pXRD data for lignin, chitosan, ZL and ZLC; Langmuir and Freundlich isotherm models for adsorption; FT-IR spectra of all dyes; parameters of adsorption kinetics, and physicochemical parameters of real water samples. See DOI: https://doi.org/10.1039/d5va00282f.

Acknowledgements

The authors thank the Swedish Foundation for Strategic Environmental Research (Mistra) for their financial support (project name Mistra TerraClean, project number 2015/31). Fei Ye and Joydeep Dutta, Functional materials, Applied Physics, KTH, are thanked for providing access to and assistance with Inductively coupled plasma optical emission spectrometry. Tove Mallin, RISE, Sweden, and Linda Önnby, IVL, Sweden, are thanked for providing PFAS-spiked water samples and for the analysis of PFAS concentration. Aji Mathew and Varvara Apostolopoulou are thanked for the instrumentation used at Stockholm University. Matthew Fielden, KTH is thanked for assistance with XPS. Master's students Helina Tafesse Belachew and Kaveri Mani are thanked for their assistance in the experiments and sample analysis. Boliden is thanked for providing mining wastewater samples.

References

1 N. A. A. Qasem, R. H. Mohammed and D. U. Lawal, *npj Clean Water*, 2021, **4**, 1–15.
2 G. Sigmund, M. Venier, M. Ågerstrand, I. T. Cousins, J. DeWitt, M. L. Diamond, J. Field, A. T. Ford, S. Joudan, S. van Leeuwen, R. Lohmann, C. Ng, M. Scheringer, A. Soehl, N. Suzuki, X. Trier, S. Valsecchi, P. Vlahos, C. J. Young and Z. Wang, *Environ. Sci. Technol. Lett.*, 2025, **12**(9), 1104–1106, DOI: 10.1021/ACS.ESTLETT.5C00478.
3 S. Mantripragada, S. O. Obare and L. Zhang, *Acc. Chem. Res.*, 2023, **56**, 1271–1278.
4 N. K. Khalid, A. Aker, S. Sť, S. Lair, S. ´Ebastien Sauvé and S. Sauvé, *Environ. Sci. Adv.*, 2025, **4**, 1599–1611, DOI: 10.1039/D5VA00061K.
5 C. Ching, Z. W. Lin, W. R. Dichtel and D. E. Helbling, *ACS ES&T Eng.*, 2023, **3**, 661–670.
6 S. Mukherjee, J. Shantha Kumar, A. Nagar and T. Pradeep, *ACS Symp. Ser.*, 2022, **1412**, 625–657.
7 M. Ahmed, M. O. Mavukkandy, A. Giwa, M. Elektorowicz, E. Katsou, O. Khelifi, V. Naddeo and S. W. Hasan, *npj Clean Water*, 2022, **5**, 1–25.

8 E. Barry, R. Burns, W. Chen, G. X. De Hoe, J. M. M. De Oca, J. J. De Pablo, J. Dombrowski, J. W. Elam, A. M. Felts, G. Galli, J. Hack, Q. He, X. He, E. Hoenig, A. Iscen, B. Kash, H. H. Kung, N. H. C. Lewis, C. Liu, X. Ma, A. Mane, A. B. F. Martinson, K. L. Mulfort, J. Murphy, K. Mølhave, P. Nealey, Y. Qiao, V. Rozyyev, G. C. Schatz, S. J. Sibener, D. Talapin, D. M. Tiede, M. V. Tirrell, A. Tokmakoff, G. A. Voth, Z. Wang, Z. Ye, M. Yesibolati, N. J. Zaluzec and S. B. Darling, *Chem. Rev.*, 2021, **121**, 9450–9501.

9 A. J. Ragauskas, G. T. Beckham, M. J. Biddy, R. Chandra, F. Chen, M. F. Davis, B. H. Davison, R. A. Dixon, P. Gilna, M. Keller, P. Langan, A. K. Naskar, J. N. Saddler, T. J. Tschaplinski, G. A. Tuskan and C. E. Wyman, *Science*, 2014, **344**(6185), 1246843, DOI: 10.1126/SCIENCE.1246843.

10 X. Liu, X. Duan, W. Wei, S. Wang and B. J. Ni, *Green Chem.*, 2019, **21**, 4266–4289.

11 M. Fazeli, S. Mukherjee, H. Baniasadi, R. Abidnejad, M. Mujtaba, J. Lipponen, J. Seppälä, O. J. Rojas and O. J. Rojas, *Green Chem.*, 2024, **26**, 593–630.

12 S. K. Lau and W. F. Yong, *ACS Appl. Polym. Mater.*, 2021, **3**, 4390–4412.

13 G. Liu, C. Matindi, M. Hu, X. Li, X. Ma and J. Li, *60 Years Loeb-Sourirajan Membr. Princ. New Mater. Model. Charact. Appl.*, 2022, 349–389.

14 D. Georgouvelas, H. N. Abdelhamid, J. Li, U. Edlund and A. P. Mathew, *Carbohydr. Polym.*, 2021, **264**, 118044.

15 L. An, Y. H. Yu, J. Chen, J. H. Bae, D. H. Youn, H. M. Jeong and Y. S. Kim, *Ind. Crops Prod.*, 2021, **167**, 113514.

16 V. Nair, A. Panigrahy and R. Vinu, *Chem.–Eng. J.*, 2014, **254**, 491–502.

17 S. Sohni, R. Hashim, H. Nidaullah, J. Lamaming and O. Sulaiman, *Int. J. Biol. Macromol.*, 2019, **132**, 1304–1317.

18 Y. Guo, W. Gao, F. Kong and P. Fatehi, *Int. J. Biol. Macromol.*, 2019, **140**, 429–440.

19 Pierce™ Bradford Protein Assay Kit, https://www.thermofisher.com/order/catalog/product/23200, accessed 14 July 2024.

20 N. B. Colthup, L. H. Daly and S. E. Wiberley, *Introd. to Infrared Raman Spectrosc.*, 1975, **341**, 321–334.

21 T. A. Saleh, *Interface Sci. Technol.*, 2022, **34**, 65–97.

22 J. Wang, L. Zhao, W. Duan, L. Han and Y. Chen, *Ind. Eng. Chem. Res.*, 2012, **51**, 13655–13662.

23 L. Ramrakhiani, S. Ghosh, S. Sarkar and S. Majumdar, *Mater. Today Proc.*, 2016, **3**, 3538–3552.

24 J. W. Heo, L. An, M. S. Kim, D. H. Youn and Y. S. Kim, *Int. J. Biol. Macromol.*, 2023, **253**, 127421.

25 M. Szabó, J. Kalmár, T. Ditrói, G. Bellér, G. Lente, N. Simic and I. Fábián, *Inorganica Chim. Acta*, 2018, **472**, 295–301.

26 O. Tkachenko, D. Diment, D. Rigo, M. Strømme and T. M. Budnyak, *Biomacromolecules*, 2024, **25**, 4292–4304.

27 O. V. Ovchinnikov, A. V. Evtukhova, T. S. Kondratenko, M. S. Smirnov, V. Y. Khokhlov and O. V. Erina, *Vib. Spectrosc.*, 2016, **86**, 181–189.

28 A. A. M. Farag and I. S. Yahia, *Opt. Commun.*, 2010, **283**, 4310–4317.

29 W. Xiao, Z. N. Garba, S. Sun, I. Lawan, L. Wang, M. Lin and Z. Yuan, *J. Clean. Prod.*, 2020, **253**, 119989.

30 L. Wu, X. Liu, G. Lv, R. Zhu, L. Tian, M. Liu, Y. Li, W. Rao, T. Liu and L. Liao, *Sci. Reports*, 2021, **11**, 1–11.

31 K. Akansha, D. Chakraborty and S. G. Sachan, *Biocatal. Agric. Biotechnol.*, 2019, **18**, 101044.

32 P. Veerakumar, T. Jeyapragasam, S. Surabhi, K. Salamalai, T. Maiyalagan and K. C. Lin, *J. Chem. Eng. Data*, 2019, **64**, 1305–1321.

33 C. M. Xing, F. N. Meng, M. Quan, K. Ding, Y. Dang and Y. K. Gong, *Acta Biomater.*, 2017, **59**, 129–138.

34 R. Xie, H. Wang, Y. Chen and W. Jiang, *Environ. Prog. Sustain. Energy*, 2013, **32**, 688–696.

35 S. Choudhary, V. Goyal and S. Singh, *Clean Technol. Environ. Policy*, 2015, **17**, 1039–1051.

36 P. S. Prasad, T. Gomathi, P. N. Sudha, M. Deepa, K. Rambabu and F. Banat, *Environ. Technol. Innov.*, 2022, **28**, 102741.

37 D. Li, X. Tian, Z. Wang, Z. Guan, X. Li, H. Qiao, H. Ke, L. Luo and Q. Wei, *Chem.–Eng. J.*, 2020, **383**, 123127.

38 X. Luo and L. Zhang, *J. Hazard. Mater.*, 2009, **171**, 340–347.

39 A. H. Jawad, A. S. Abdulhameed, S. N. Surip and Z. A. Alothman, *J. Clean. Prod.*, 2023, **393**, 136334.

40 Ł. Klapiszewski, K. Siwińska-Stefańska and D. Kołodyńska, *Chem.–Eng. J.*, 2017, **330**, 518–530.

41 B. Du, L. Chai, Q. Zheng, Y. Liu, X. Wang, X. Chen, S. Zhai, J. Zhou and R. C. Sun, *Int. J. Biol. Macromol.*, 2023, **234**, 123668.

42 A. L. Popovic, J. D. Rusmirovic, Z. Velickovic, Z. Radovanovic, M. Ristic, V. P. Pavlovic and A. D. Marinkovic, *Int. J. Biol. Macromol.*, 2020, **156**, 1160–1173.

43 B. Du, W. Li, L. Chai, W. Li, X. Wang, X. Chen, J. Zhou and R. C. Sun, *J. Mol. Liq.*, 2023, **377**, 121566.

44 C. Jiang, X. Wang, D. Qin, W. Da, B. Hou, C. Hao and J. Wu, *J. Hazard. Mater.*, 2019, **369**, 50–61.

45 J. Chen, J. Wu, Y. Zhong, X. Ma, W. Lv, H. Zhao, J. Zhu and N. Yan, *Sep. Purif. Technol.*, 2023, **311**, 123284.

46 A. Mahto, A. Kumar, J. P. Chaudhary, M. Bhatt, A. K. Sharma, P. Paul, S. K. Nataraj and R. Meena, *J. Hazard. Mater.*, 2018, **353**, 190–203.

47 D. Li, C. S. Lee, Y. Zhang, R. Das, F. Akter, A. K. Venkatesan and B. S. Hsiao, *J. Mater. Chem. A*, 2023, **11**, 9868–9883.

48 C. He, Y. Yang, Y. J. Hou, T. Luan and J. Deng, *Sep. Purif. Technol.*, 2022, **294**, 121195.

49 I. M. Militao, F. Roddick, L. Fan, L. C. Zepeda, R. Parthasarathy and R. Bergamasco, *J. Water Process Eng.*, 2023, **53**, 103616.

50 S. S. Elanchezhiyan, J. Preethi, K. Rathinam, L. K. Njaramba and C. M. Park, *Carbohydr. Polym.*, 2021, **267**, 118165.

51 D. Xiao, W. Dong, H. Wang, J. Cao, J. Liu, Y. Wang, Y. Wu, F. Ma and H. Yi, *Chem.–Eng. J.*, 2025, **519**, 164887.

52 H. V. Patel, M. Greer, B. Brazil, W. Yu, S. Hamoush, L. Zhang and R. Zhao, *J. Hazard. Mater.*, 2025, **484**, 136763.

53 A. Chaudhary, M. Usman, O. Mašek, S. Haderlein and K. Hanna, *J. Water Process Eng.*, 2025, **74**, 107875.

54 R. Mailler, O. Danel, M. Esperanza, S. Courtois and A. Gonzalez Ospina, *Sci. Total Environ.*, 2024, **952**, 175918.

55 Y. Zhang, K. Kong, Q. Wu, T. Ma, J. Liang and R. Wang, *ChemSusChem*, 2024, **17**, e202400069.